

# Upconverting Nanoparticles as Optical Sensors of Nano- to Micro-Newton Forces

Alice Lay,<sup>\*,†</sup> Derek S. Wang,<sup>‡</sup> Michael D. Wisser,<sup>‡</sup> Randy D. Mehlenbacher,<sup>‡</sup> Yu Lin,<sup>§</sup> Miriam B. Goodman,<sup>||</sup> Wendy L. Mao,<sup>⊥</sup> and Jennifer A. Dionne<sup>\*,‡</sup>

<sup>†</sup>Department of Applied Physics, <sup>‡</sup>Department of Materials Science and Engineering, <sup>||</sup>Department of Molecular and Cellular Physiology, <sup>⊥</sup>Department of Geological Sciences, Stanford University, Stanford, California 94305, United States

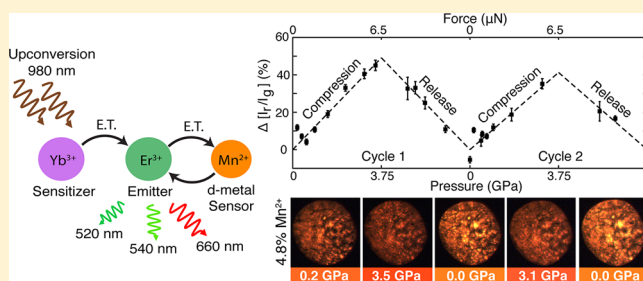
<sup>§</sup>Stanford Institute for Materials and Energy Sciences, SLAC National Accelerator Laboratory, Menlo Park, California 94025, United States

## S Supporting Information

**ABSTRACT:** Mechanical forces affect a myriad of processes, from bone growth to material fracture to touch-responsive robotics. While nano- to micro-Newton forces are prevalent at the microscopic scale, few methods have the nanoscopic size and signal stability to measure them in vivo or in situ. Here, we develop an optical force-sensing platform based on sub-25 nm NaYF<sub>4</sub> nanoparticles (NPs) doped with Yb<sup>3+</sup>, Er<sup>3+</sup>, and Mn<sup>2+</sup>. The lanthanides Yb<sup>3+</sup> and Er<sup>3+</sup> enable both photoluminescence and upconversion, while the energetically coupled *d*-metal Mn<sup>2+</sup> adds force tunability through its crystal field sensitivity.

Using a diamond anvil cell to exert up to 3.5 GPa pressure or ~10 μN force per particle, we track stress-induced spectral responses. The red (660 nm) to green (520, 540 nm) emission ratio varies linearly with pressure, yielding an observed color change from orange to red for α-NaYF<sub>4</sub> and from yellow–green to green for *d*-metal optimized β-NaYF<sub>4</sub> when illuminated in the near infrared. Consistent readouts are recorded over multiple pressure cycles and hours of illumination. With the nanoscopic size, a dynamic range of 100 nN to 10 μN, and photostability, these nanoparticles lay the foundation for visualizing dynamic mechanical processes, such as stress propagation in materials and force signaling in organisms.

**KEYWORDS:** Upconversion, lanthanides, diamond anvil cell, crystal field theory, *d*-metal, force sensor



Mechanical forces play a critical role in multiple fields, including robotics, materials science, and biology. Skin-mimetic devices, for example, utilize organic field effect transistors and piezoresistive materials to replicate the sense of touch for machine–human interfaces.<sup>1</sup> Meanwhile, layered polymeric nanocomposites can arrest speeding bullets by dissipating large strains upon impact, paving the way for new armor and bulletproof vests.<sup>2</sup> Even our cells act as force transducers. Mechanical cues from the extracellular matrix regulate biological processes, such as stem cell differentiation and tissue organization.<sup>3</sup> Indeed, improper sensing and mechanotransduction underly many diseases, including some cancers, osteoporosis, and heart disease.<sup>4</sup>

There is a growing interest and need for tools that measure mechanical forces. Currently, mechanical behavior is mainly characterized by external probing techniques, including atomic force microscopy (AFM), traction force microscopy (TFM), and optical tweezing. To probe forces within electronic, material, and biological systems, sensing platforms with reduced dimensions are required. Recent developments include micron-sized oil droplets,<sup>5</sup> graphene films,<sup>6</sup> and carbon nanotube devices.<sup>7</sup> However, further reduction in size and elimination of external electronic components are still needed to reduce invasiveness for in vivo and in situ applications. Nanoparticles have gained

increasing interest, due to their high tunability in size, morphology, composition, and surface chemistry. Promising platforms include semiconducting quantum dots<sup>8</sup> and tetrapods,<sup>9,10</sup> which yield a spectral shift upon force application, though their cytotoxicity remains a key concern for biospecimens.<sup>11,12</sup> Additionally, plasmonic rulers that rely on coupling between metallic nanoparticles to measure DNA stiffnesses<sup>13</sup> may be refashioned to study tension. The majority of current sensors actually consist of fluorophores (e.g., porphyrin-based molecular rotors<sup>14</sup>), and of these, Förster resonance energy transfer (FRET)-based sensors are the most sensitive for in vivo applications. FRET sensors excel at measuring 1–10 piconewton forces.<sup>15</sup> However, their readout is based solely on intensity, which can be convoluted with blinking, cross-talk, and photobleaching over several minutes.<sup>16</sup> Additionally, FRET sensors are limited in their ability to sense larger, nano-Newton (nN) to micro-Newton (μN) forces. Examples of forces in this range abound in nature, such as those exerted by gecko foot-hairs to climb up walls (up to 20 μN),<sup>17</sup> contracting bundles of skeletal

Received: March 7, 2017

Revised: June 2, 2017

Published: June 13, 2017

muscle myofibrils ( $\sim 0.7 \mu\text{N}$ ),<sup>18</sup> and focal adhesions that anchor cells to their substrates (1–2 pN to 30 nN).<sup>19,20</sup>

As these studies have illustrated, optical force sensors are especially promising because they provide high spatial resolution, minimize direct interference with samples, and complement advanced microscopy techniques. Here, we improve the dynamic range, robustness of readout, and ease of integration of optical force sensors. Specifically, we design *d*-metal and lanthanide-doped nanoparticles with (1) sensitivity in the nN to  $\mu\text{N}$  range, (2) stable spectral (i.e., color) readout, and (3) nanoscopic size for future high resolution in situ and in vivo applications. These nanoparticles leverage the sensitivity of *d*-metal ions (i.e.,  $\text{Mn}^{2+}$ ) to the external crystal field, a phenomenon that explains the rich colors characteristic of transition metal complexes.<sup>21</sup> Simultaneously, lanthanide ions (i.e.,  $\text{Yb}^{3+}$  and  $\text{Er}^{3+}$ ) perform both photoluminescence (PL) and upconversion (UC) when excited in the visible or near-infrared (NIR), respectively. Our experiments show that these nanoparticles exhibit sharp Stokes and anti-Stokes emission peaks, tunability with *d*-metal doping and external forces, and photostability for over 24 h. Additionally, because of their low toxicity and absorption within the biological transparency window, these upconverters can enable background-free, deep-tissue imaging.<sup>22–24</sup> As force sensors, these nanoparticles offer both color and intensity readouts in UC and PL. Such multimodal reporting is versatile and unique compared to currently available optical sensors, which primarily have intensity readouts and require averaging intensity changes over many measurements.

We use  $\text{NaYF}_4$  as the host lattice for our force-sensing nanoparticles, as it supports efficient lanthanide-based upconversion.<sup>25</sup> Furthermore, the material has two phases, cubic ( $\alpha$ ) and hexagonal ( $\beta$ ), which are characterized by distinct symmetries. As seen in Figure 1a, in  $\alpha$ - $\text{NaYF}_4$ ,  $\text{Y}^{3+}$  ions are surrounded by a centrosymmetric, cubic  $\text{F}^-$ -ligand environment. In  $\beta$ - $\text{NaYF}_4$ ,  $\text{Y}^{3+}$  ions are surrounded by  $\text{F}^-$  ions in a noncentrosymmetric, trigonal tricapped prismatic geometry.<sup>26</sup> For dual UC and PL capabilities, the sensitizer,  $\text{Yb}^{3+}$ , and emitter,  $\text{Er}^{3+}$ , are incorporated into the host lattice, where they substitute  $\text{Y}^{3+}$ .<sup>27,28</sup> To achieve nN to  $\mu\text{N}$  sensitivity, we substitute  $\text{Y}^{3+}$  for the *d*-metal ion,  $\text{Mn}^{2+}$  (Figure 1a). In our system, schematically portrayed in Figure 1c,  $\text{Mn}^{2+}$  acts as a pressure sensor to the lanthanide pair.  $\text{Mn}^{2+}$  is coupled to the  $\text{Er}^{3+}$  green and red emission peaks (centered about 520 nm ( $g_1$ ), 540 nm ( $g_2$ ), and 660 nm ( $r$ )) and provides an alternative energetic pathway which siphons would-be photons from  $\text{Er}^{3+}$  green states into the red state.<sup>29</sup> As a result, external forces will not only alter the external crystal field of  $\text{Mn}^{2+}$ , but also the energy transfer processes, thereby changing the relative intensities of  $g_1$ ,  $g_2$ , and  $r$  in the emission spectra for both UC and PL. A detailed energy level diagram and analysis can be found in the Supporting Information (SI). Further, because stress-induced strain of the crystal lattice breaks local symmetry,<sup>30</sup> we expect that  $\alpha$ - $\text{NaYF}_4$  will have different optical properties and pressure sensitivity than  $\beta$ - $\text{NaYF}_4$ .

Sub-25 nm  $\text{Mn}^{2+}$ -doped  $\text{NaYF}_4:\text{Er}^{3+},\text{Yb}^{3+}$  nanoparticles are prepared by modifying a hydrothermal autoclave synthesis<sup>29,31</sup> for  $\alpha$ -phase NPs and a one-pot colloidal synthesis<sup>32</sup> for  $\beta$ -phase NPs. These techniques produce monodisperse nanoparticles with 18%  $\text{Yb}^{3+}$ , 2%  $\text{Er}^{3+}$ , and controlled  $\text{Mn}^{2+}$ -doping ranging from 0% to 5%, as confirmed by inductively coupled plasma optical emission spectroscopy. To prevent mixed-phase samples and maintain fixed lanthanide concentrations, we did not investigate NPs beyond 4.8%  $\text{Mn}^{2+}$  for  $\alpha$ - $\text{NaYF}_4$  and 1.5%  $\text{Mn}^{2+}$  for  $\beta$ - $\text{NaYF}_4$ . Note that  $\text{Mn}^{2+}$  incorporation is typically easier and more

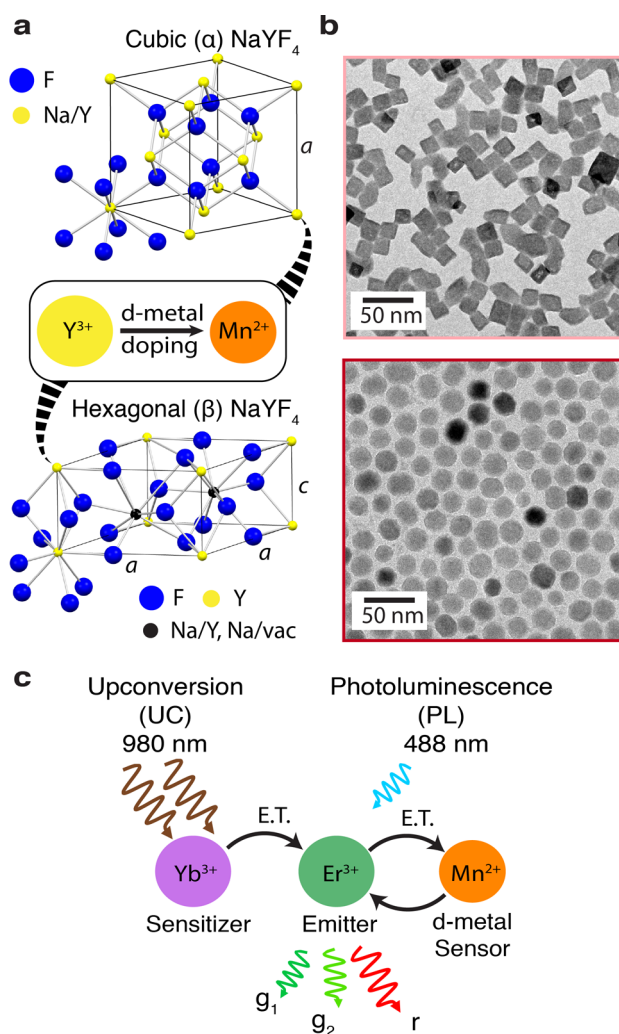


**Figure 1.** Structure and mechanism of optical sensors. (a) Crystal structure of cubic ( $\alpha$ )  $\text{NaYF}_4$  unit cell and hexagonal ( $\beta$ )  $\text{NaYF}_4$  unit cell.  $\text{Mn}^{2+}$  substitutes  $\text{Y}^{3+}$  sites within the host lattice. (b) Representative transmission electron microscope (TEM) images show the morphology and size of  $\text{Mn}^{2+}$ -doped cubic (top) and hexagonal (bottom) nanoparticles. (c) Schematic showing the interaction between lanthanide and *d*-metal ions: in upconversion (UC),  $\text{Yb}^{3+}$  acts as the sensitizer to absorb multiple NIR (980 nm) photons and transfers energy to  $\text{Er}^{3+}$ .  $\text{Er}^{3+}$  acts as the emitter and produces emission peaks at green ( $g_1$ ,  $g_2$ ) and red ( $r$ ) visible wavelengths.  $\text{Mn}^{2+}$ -doping introduces additional crystal field sensitivity and a new energetic pathway with forward and backward energy transfer (ET) between  $\text{Er}^{3+}$  and  $\text{Mn}^{2+}$ . In photoluminescence (PL), higher energy photons (488 nm) populate  $\text{Er}^{3+}$  and  $\text{Mn}^{2+}$  states to yield traditional Stokes emission.

consistent in  $\alpha$ -phase than  $\beta$ -phase NPs due to differences in cation site symmetries. Representative transmission electron microscope (TEM) images in Figure 1b show cubes with edge lengths of  $17.3 \pm 3.6$  nm for  $\alpha$ -NPs and spheres with radii of  $10.5 \pm 1.2$  nm for  $\beta$ -NPs. Across all  $\text{Mn}^{2+}$ -doping concentrations investigated, we not only achieve similar size and uniformity, but also phase purity. Additional details on the synthesis, composition, and structure of these nanoparticles can be found in the SI.

First, we characterize the effects of  $\text{Mn}^{2+}$ -doping on UC and PL emission under ambient, pre-stress conditions. Figure 2a displays the UC (dashed) and PL (solid) spectra of dropcasted NPs for both the  $\alpha$ - and  $\beta$ -series. Here, each spectrum is normalized to its

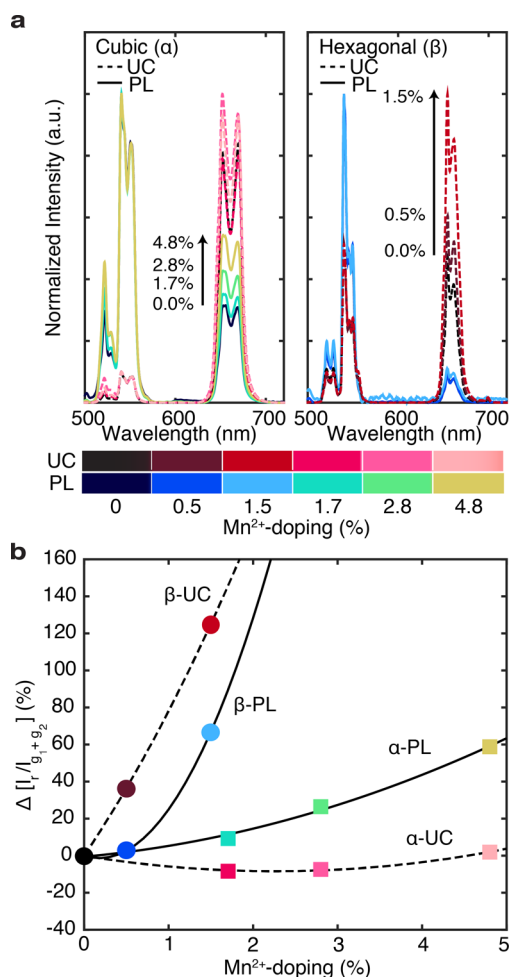


**Figure 2.** Effect of *d*-metal doping on optical properties. (a) Overlay of UC (dashed) and PL (solid) spectra of cubic and hexagonal UCNPs with varying Mn<sup>2+</sup>-doping concentration. Each spectrum is normalized to its *g*<sub>2</sub> emission peak to spectrally visualize the red to green ratio  $\frac{I_r}{I_{g_1+g_2}}$ . Note that UC and PL spectra are scaled differently due to variations in relative peak heights for *g*<sub>1</sub>, *g*<sub>2</sub>, and *r*. “Black to pink” and “blue to yellow” colors bars represent varying Mn<sup>2+</sup>-doping for UC and PL, respectively. Lighter colors are associated with higher Mn<sup>2+</sup>-doping concentrations. (b) Summary of percent change in  $\frac{I_r}{I_{g_1+g_2}}$  from controls (0% Mn<sup>2+</sup>) with respect to Mn<sup>2+</sup>-doping concentration. Guides-to-the-eye show the different optical effects of Mn<sup>2+</sup>-doping in α-NaYF<sub>4</sub> (squares) versus β-NaYF<sub>4</sub> (circles). Errors associated with the resolution of the spectrometer grating are within the markers (see SI).

own *g*<sub>2</sub> peak in order to display the relative changes in the red peak. Due to differences in peak heights, the UC and PL spectra are scaled independently. For both phases, increasing Mn<sup>2+</sup>-doping enhances the relative red emission. These spectral effects are summarized in Figure 2b as the percent change in the red to green ratio; the red to green ratio,  $\frac{I_r}{I_g}$ , is defined as the integrated intensity of red emission, *r*, divided by that of the green emission peaks, *g*<sub>1</sub> and *g*<sub>2</sub>. Notably, β-NPs show a more pronounced enhancement of red emission with increasing Mn<sup>2+</sup>-doping. This β-NaYF<sub>4</sub> lattice has lower  $\frac{I_r}{I_g}$  (and hence relatively higher population of the green state) than α-NaYF<sub>4</sub>, meaning that there are more available photons for Mn<sup>2+</sup>, upon introduction, to shuttle into the red state. Another factor is synthetically induced strain from doping, which

leads to external crystal field distortions. Fits of X-ray diffraction data indicate greater strain on the lattice parameters in the β-series (up to 0.32%) compared to the lattice parameter in the α-series (up to 0.10%) (see Figure S2).

Next, we characterize the force sensitivity of each type of nanoparticle using a laser-coupled diamond anvil cell (DAC) setup. Briefly, the DAC contains two diamond culets that mechanically compress NPs in a quasi-hydrostatic pressure environment with silicone oil. Meanwhile, a bulk ruby sphere enables pressure calibration.<sup>33</sup> Increasing compression incrementally up to ~3.5 GPa to probe the nano- to micro-Newton force regime, we collect UC and PL spectra. Optical images are also obtained on a digital camera to qualitatively visualize changes in emission, including color and intensity. Intensity responses, which are generally characterized by a decrease in photon counts with increasing pressure, are detailed fully in the SI. We focus here on color responses because they are especially robust to systematic errors, such as sample or source fluctuations.

We track the change in emission color, or, more quantitatively, the percent change in the red to green ratio from the ambient condition,  $\Delta \frac{I_r}{I_g}$  (%). Figure 3a and b display our UC and PL DAC measurements for one pressure cycle of compression (filled points) and release (open points). A representative force range of the studied pressures is derived using the total surface area of the α-4.8% NPs and listed on the top *x*-axis. Average  $\Delta \frac{I_r}{I_g}$  (%) values are recorded with error bars indicating the spread of three spectra collected at each pressure point. Linear error-weighted least-squares fits of the data are also graphed; the slope,  $\Delta \frac{I_r}{I_g}$  (% per GPa), quantifies the color change induced by one GPa of applied pressure and represents the pressure sensitivity of the nanoparticles.

In UC (Figure 3a),  $\frac{I_r}{I_{g_1+g_2}}$  values of α-NPs show a positive linear response to pressure. In other words, they get “redder.” This trend can be visually perceived for the most sensitive of the α-series, 4.8% Mn<sup>2+</sup> (Figure 3c). Comparing the emission color at ambient pressure and maximum pressure, 3.5 GPa, there is a difference in perceived color, from orange to red. In contrast, β-UCNPs show a constant (i.e., no color change) or slightly negative (i.e., “greener”) linear response to pressure. In the most sensitive of the β-series, 1.5% Mn<sup>2+</sup>, the optical images at 0.0 and 2.9 GPa also show a perceived change, from yellow–green to green. For PL (Figure 3b), we probe the red to green ratio,  $\frac{I_r}{I_{g_2}}$ , excluding the *g*<sub>1</sub> peak, because the Raman spectrum of diamond at 488 nm interferes with Er<sup>3+</sup> emission at ~520 nm.<sup>34</sup> For both phases, the fits of PL data have positive slopes. Representative spectra for α-4.8% and β-1.5% are displayed in Figure 3d and f, respectively. Each spectrum at loading pressure (black), maximum pressure (blue), and full release of pressure (red) is normalized to its *g*<sub>2</sub> peak to see relative shifts in the *r* peak. Noticeably, the change in red emission is much greater for UC spectra than PL spectra, which coincides with the qualitative results of the corresponding optical images.

Figure 4a summarizes the slopes or pressure sensitivity,  $\Delta \frac{I_r}{I_g}$  (% per GPa), for all nanoparticles. NPs get “redder” with pressure in the red-shaded region, while NPs get “greener” with pressure in the green-shaded region. We evaluate UC and PL data separately, given that ambient  $\frac{I_r}{I_g}$  values are nearly 10× higher for UC (see

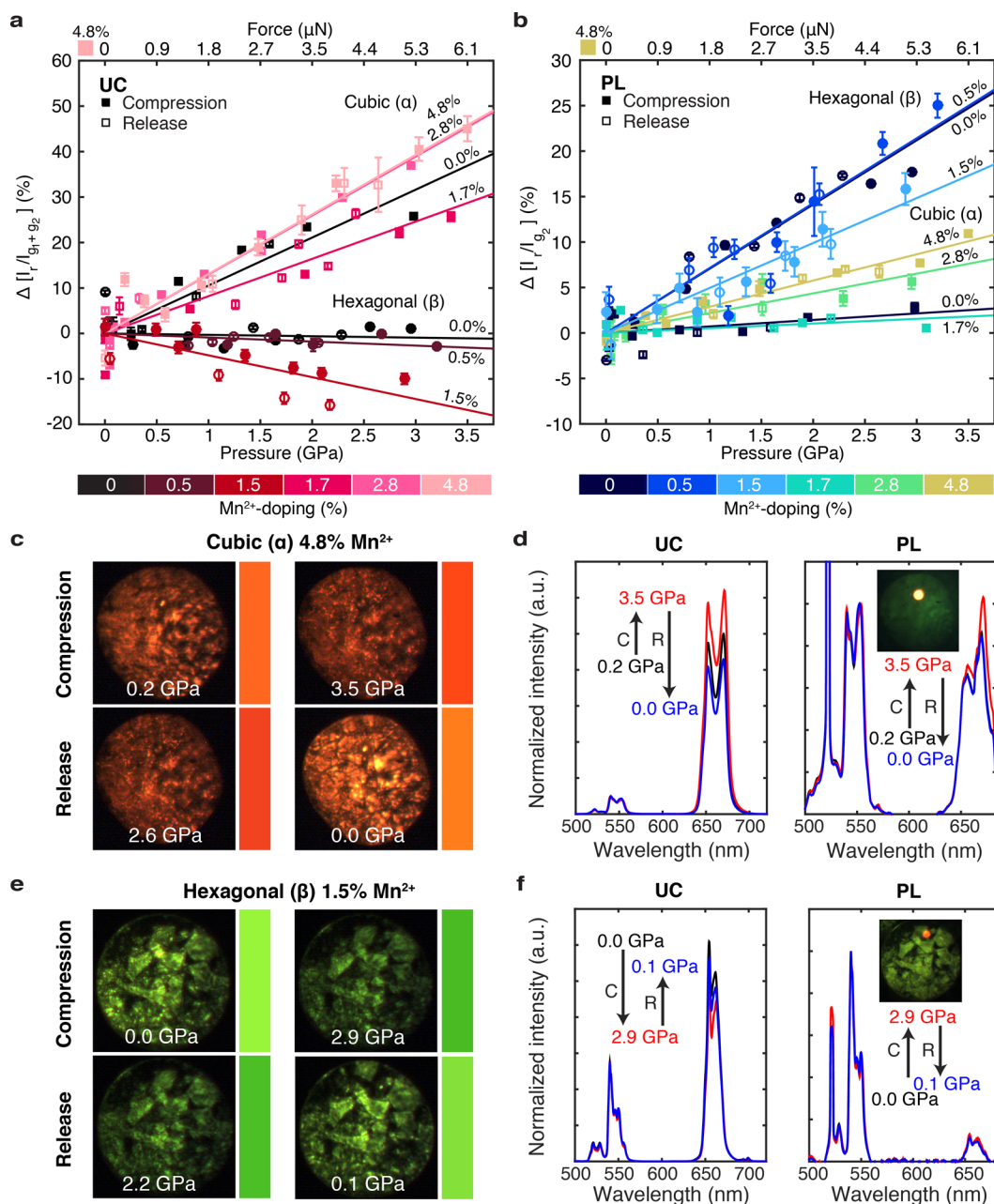


**Figure 3.** Color response of nanoparticles under pressure. Top graphs show (a) UC and (b) PL diamond anvil cell (DAC) measurements from one complete pressure cycle for all particles in the  $\alpha$ - and  $\beta$ -series, represented by square and circle markers, respectively. Error bars represent the standard deviation of  $\frac{I_r}{I_g}$  values, derived from three spectra collected at each pressure point (see the SI). Error-weighted linear fits of the compression (filled) and release (open) points are graphed; their slopes represent the pressure sensitivity,  $\Delta \frac{I_r}{I_g}$  (% per GPa). Note that the red to green ratio is  $\frac{I_r}{I_{g_1+g_2}}$  for UC and  $\frac{I_r}{I_{g_2}}$  for PL. A representative force scale is listed on the top axis for  $\alpha$ -4.8% NPs, which corresponds to the higher magnitude of forces between the two phases. Optical images of UC in the most sensitive nanoparticles, (c)  $\alpha$ -4.8% and (e)  $\beta$ -1.5%, are displayed at select pressure points during compression (top) and release (bottom). The circular area of luminescence is determined by the size of the DAC sample chamber,  $\sim 300 \mu\text{m}$  in diameter. The images, with adjacent color swatches, qualitatively show intensity and color responses. UC and PL spectra in panels (d) and (f) represent spectra at the loading (black), maximum (red), and ambient release (blue) pressures. Each spectrum is normalized to its  $g_2$  peak to see the relative red enhancement ( $\alpha$ -4.8%) or decrease ( $\beta$ -1.5% UC) with pressure. Arrows indicate the direction of relative change upon compression (C) and then release (R). A representative PL image (inset) shows the green emission from the nanoparticles, as well as orange emission from the bulk ruby.

Tables S6–S9 and Figure S12). This analysis yields several conclusions. First in UC,  $\alpha$ -NPs are more responsive to pressure than  $\beta$ -NPs. We consider a color change in the red (positive) or green (negative) direction to be equally valuable. At comparable  $\text{Mn}^{2+}$ -doping concentrations (i.e., in the 0–1.5% doping range), the  $\alpha$ -phase UC sensitivity value is at least  $1.7\times$  that of the  $\beta$ -phase

counterpart. These results are consistent with expectations that UC in  $\alpha$ - $\text{NaYF}_4$  is more susceptible to external crystal field modulation.<sup>30</sup> The  $10.5 \pm 1.1\%$  per GPa value for the 0% case also suggests that pressure sufficiently alters the energetics of the upconverting pair,  $\text{Yb}^{3+}$  and  $\text{Er}^{3+}$ , for a nontrivial color response in  $\alpha$ -UC. Conversely, the lanthanide ions are nearly insensitive to

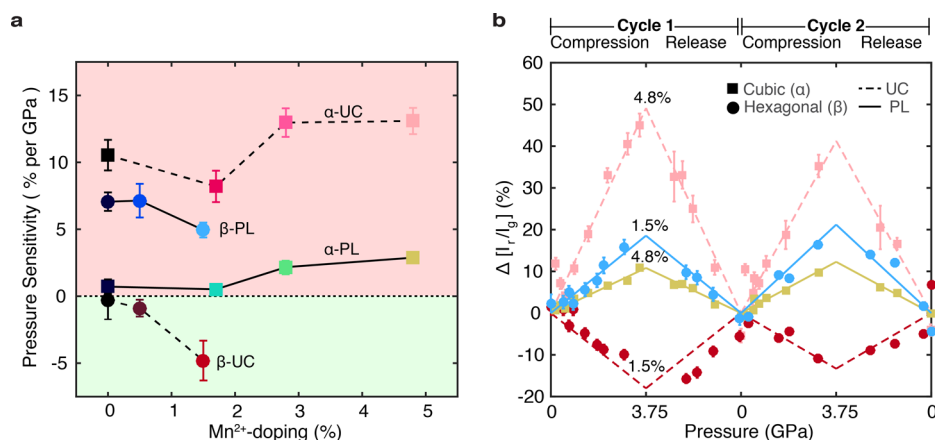


**Figure 4.** Pressure sensitivity and cyclability of optical sensors. (a) Pressure sensitivity or percent change in the red to green ratio,  $\Delta \frac{I_r}{I_g}$  (%), due to one GPa of applied pressure. Data points in the red- or green-shaded region indicate NPs that exhibit a positive (“redder”) or negative (“greener”) linear response with pressure. We weigh the color change in either direction equally as an optical readout for pressure. Error bars represent half of the 95% confidence interval for the fitted slopes in Figure 3 (see SI). (b) DAC pressure measurements for two cycles of compression and release on samples with highest Mn<sup>2+</sup>-doping concentrations,  $\alpha$ -4.8% and  $\beta$ -1.5%. Error-weighted linear fits are determined for each cycle using both compression and release data points, as in Figure 3a and b. Error bars may be obscured by markers. The pressure sensitivity (i.e., slope) of Cycle 2 is typically within the error of Cycle 1 (see SI).

pressure in  $\beta$ -0% NPs at  $-0.3 \pm 1.4\%$  per GPa. From these observations, it is clear that with or without the *d*-metal sensor, the two crystal phases have different mechano-optical behavior within micro-Newton force regimes. Second, higher Mn<sup>2+</sup>-doping concentrations generally increase the average pressure sensitivity in UC. We explain possible reasons for the initial decrease for  $\alpha$ -1.7% in the SI. The enhancement is most pronounced in the  $\beta$ -series, where 1.5% doping introduces sensitivity to NPs that would, without the *d*-metal sensor, not yield any color response upon mechanical stimuli. Specifically, the pressure sensitivity increases nearly 16-fold from  $-0.3 \pm 1.4\%$  per GPa to  $-4.8 \pm 1.5\%$  per GPa. In the  $\alpha$ -series, a maximum sensitivity of  $13.1 \pm 1.0\%$  per GPa is achieved at 4.8% doping, yielding a 1.25 $\times$  improvement from undoped particles. This difference in the added benefit of Mn<sup>2+</sup>-doping on sensitivity supports our earlier findings (Figure 2) that Mn<sup>2+</sup> is more energetically coupled to Er<sup>3+</sup> emission in  $\beta$ -NaYF<sub>4</sub> than  $\alpha$ -NaYF<sub>4</sub>. Additionally, while Mn<sup>2+</sup> pushes sensitivity of the  $\beta$ -NPs toward the green region, it does the opposite for  $\alpha$ -NPs (seen consistently in both UC and PL trends). This result suggests that pressure increases coupling between Er<sup>3+</sup> and Mn<sup>2+</sup> for the  $\alpha$ -phase NPs and decreases coupling for the  $\beta$ -phase NPs, with increasing pressure. Additional details and proposed energetics can be found in the SI.

We test the performance of our force-sensing technology over multiple pressure cycles to characterize the robustness of the optical readouts. Figure 4b shows the percent change in  $\frac{I_r}{I_g}$  for representative  $\alpha$ -4.8% and  $\beta$ -1.5% NPs over two measurement cycles; up to five cycles are presented in the SI. The linear fits of Cycle 2, calculated from the next set of compression and release points, are typically within the reported error of Cycle 1 (also see SI); for  $\alpha$ -4.8% UC, Cycle 2 has a sensitivity of  $11.1 \pm 1.0\%$  per GPa versus Cycle 1 at  $13.1 \pm 1.0\%$  per GPa, indicating that already-compressed NPs are nearly as sensitive as before. Not only are the linear color responses reproducible, but the ambient optical properties are also recoverable even after multiple measurements that total nearly 24 h of laser illumination. For the same pressure value, the change in ratio (i.e., emission color) is comparable along the two cycles, implying that these NPs can be implemented to estimate the magnitude of forces based on the

ratio-to-pressure relationships derived in this work. These observations are consistent for all samples in both the  $\alpha$ -NaYF<sub>4</sub> and  $\beta$ -NaYF<sub>4</sub> series (see Figures S5–S11). Further, in situ X-ray diffraction experiments and post-press TEM images confirm that we are probing the elastic regime of these nanoparticles and that no phase change or plastic deformation results (see SI). Together, these experiments demonstrate the structural and optical integrity of these force reporters.

In summary, we present a toolkit of force-sensing nanoparticles, capable of visualizing and quantifying micro-Newton forces for future in vivo and in situ applications. Compared to existing sensors, our nanoparticles offer unique capabilities, including a larger dynamic range of at least 100 nN to 10  $\mu$ N, signal stability over 24 h, and dual readouts in UC and PL, with the former being especially suitable for background-free imaging in tissue. In addition, the *d*-metal and lanthanide system is a novel stress-sensing platform based on crystal field interactions. Mn<sup>2+</sup> acts as an ionic pressure sensor, whose energetic coupling with the emitter Er<sup>3+</sup> is tunable by external pressure, leading to a perceivable and measurable color change. Since the color response is based on the ratiometric relationship between emission peaks, the readout should be less susceptible to variations in material thicknesses, instrumentation, and movement artifacts than an intensity signal. By increasing the Mn<sup>2+</sup> content, we show improved sensitivity in both crystal phases: a  $\Delta \frac{I_r}{I_g}$  (% per GPa) up to 1.25 $\times$  in  $\alpha$ -NaYF<sub>4</sub> and 16 $\times$  in  $\beta$ -NaYF<sub>4</sub>.

While our results indicate that  $\alpha$ -UC has the most sensitive color response to micro-Newton force stimuli,  $\beta$ -NPs with higher Mn<sup>2+</sup> content typically offer 10 $\times$  brighter emission.<sup>25,27,28</sup> Further optimization of force sensitivity may be achieved with other *d*-metal dopants. Fe<sup>3+</sup>, for example, is believed to be optically coupled to Er<sup>3+</sup> and because of its similar charge state to lanthanide ions, may be easier to incorporate into the NaYF<sub>4</sub> lattice.<sup>35</sup> Finally, given the sub-25 nm size, our nanoparticles promise high resolution and easy integration within synthetic and biological materials. Already, NaYF<sub>4</sub> nanoparticles of similar size and composition have been imaged in mice and cell cultures, showing minimal cytotoxicity.<sup>29,36,37</sup> In polymeric substrates like PDMS, the nanoparticles have also been embedded.<sup>38</sup> Hence,

these nanoparticles may pave the way to visualization of dynamic processes, including the propagation of stress within substrates and mechanical signaling within cells, tissue, and organisms.

## ■ ASSOCIATED CONTENT

### 📄 Supporting Information

The Supporting Information is available free of charge on the ACS Publications website at DOI: [10.1021/acs.nanolett.7b00963](https://doi.org/10.1021/acs.nanolett.7b00963).

Procedures and methods for nanoparticle syntheses, DAC measurements, data processing, and pressure-to-force conversion, characterization data (i.e., ICP-OES, TEM, XRD), DAC results for all nanoparticle samples, additional in situ XRD and pressure-cycling experiments, performance metrics (i.e., sensitivity values, dynamic range, force resolution), and further discussion and analysis of the DAC environment, intensity and color readouts, energetics, and mechanical properties of the nanoparticles (PDF)

## ■ AUTHOR INFORMATION

### Corresponding Authors

\*E-mail: [alay@stanford.edu](mailto:alay@stanford.edu).

\*E-mail: [jdionne@stanford.edu](mailto:jdionne@stanford.edu).

### ORCID

Alice Lay: 0000-0001-5179-7150

Yu Lin: 0000-0001-5174-9546

### Notes

The authors declare no competing financial interest.

## ■ ACKNOWLEDGMENTS

The authors thank Tarun Narayan, Ashwin Atre, Fan Yang, Yang Zhao, Arturas Vailionis, Guangchao Li, Katherine Sytwu, Stefan Fischer, Diane Wu, Justin Briggs, and Fariah Hayee for scientific feedback and support. A.L., D.S.W., R.D.M., M.B.G., and J.A.D. acknowledge financial support from Stanford NeuroFab and Bio-X Interdisciplinary Initiatives Committee (IIP). A.L. was supported by the NSF GRFP (2013156180). M.D.W. and J.A.D. were supported by DOE "Light-Material Interactions in Energy Conversion" Energy Frontier Research Center under grant No. DE-SC0001293. Work by Y.L. and W.L.M. was supported through the Department of Energy through the Stanford Institute for Materials & Energy Sciences DE-AC02-76SF00515. TEM imaging and XRD characterization were performed at the Stanford Nano Shared Facilities (SNSF). ICP-OES data were collected at the Environmental Measurements Facility (EMF) at Stanford University. The in situ XRD pressure experiments were performed at HPCAT (Sector 16), APS, ANL. HPCAT operations are supported by DOE-NNSA under award No. DE-NA0001974 and DOE-BES under award No. DE-FG02-99ER45775, with partial instrumentation funding by NSF. The APS is a U.S. DOE Office of Science User Facility operated for the DOE Office of Science by Argonne National Laboratory under Contract No. DE-AC02-06CH11357. All opinions expressed in this paper are the authors' and do not necessarily reflect the policies and views of NSF, DOE, and Stanford University.

## ■ REFERENCES

- (1) Chortos, A.; Liu, J.; Bao, Z. *Nat. Mater.* **2016**, *15*, 937–950.
- (2) Lee, J.-H.; Veysset, D.; Singer, J. P.; Retsch, M.; Saini, G.; Pezeril, T.; Nelson, K. A.; Thomas, E. L. *Nat. Commun.* **2012**, *3*, 1164.
- (3) Ingber, D. *Ann. Med.* **2003**, *35*, 564–577.
- (4) DuFort, C. C.; Paszek, M. J.; Weaver, V. M. *Nat. Rev. Mol. Cell Biol.* **2011**, *12*, 308–319.

- (5) Campàs, O.; Mammoto, T.; Hasso, S.; Sperling, R. A.; O'Connell, D.; Bischof, A. G.; Maas, R.; Weitz, D. A.; Mahadevan, L.; Ingber, D. E. *Nat. Methods* **2013**, *11*, 183–189.
- (6) Zhao, J.; Wang, G.; Yang, R.; Lu, X.; Cheng, M.; He, C.; Xie, G.; Meng, J.; Shi, D.; Zhang, G. *ACS Nano* **2015**, *9*, 1622–1629.
- (7) Stampfer, C.; Helbling, T.; Oberfell, D.; Schöberle, B.; Tripp, M.; Jungen, A.; Roth, S.; Bright, V.; Hierold, C. *Nano Lett.* **2006**, *6*, 233–237.
- (8) Fischer, T.; Stöttinger, S.; Hinze, G.; Bottin, A.; Hu, N.; Basché, T. *Nano Lett.* **2017**, *17*, 1559–1563.
- (9) Choi, C. L.; Koski, K. J.; Sivasankar, S.; Alivisatos, A. P. *Nano Lett.* **2009**, *9*, 3544–3549.
- (10) Choi, C. L.; Koski, K. J.; Olson, A. C.; Alivisatos, A. P. *Proc. Natl. Acad. Sci. U. S. A.* **2010**, *107*, 21306–21310.
- (11) Derfus, A. M.; Chan, W. C.; Bhatia, S. N. *Nano Lett.* **2004**, *4*, 11–18.
- (12) Tsoi, K. M.; Dai, Q.; Alman, B. A.; Chan, W. C. *Acc. Chem. Res.* **2013**, *46*, 662–671.
- (13) Chen, T.; Hong, Y.; Reinhard, B. M. *Nano Lett.* **2015**, *15*, 5349.
- (14) Kamat, N. P.; Liao, Z.; Moses, L. E.; Rawson, J.; Therien, M. J.; Dmochowski, I. J.; Hammer, D. A. *Proc. Natl. Acad. Sci. U. S. A.* **2011**, *108*, 13984–13989.
- (15) Cost, A.-L.; Ringer, P.; Chrostek-Grashoff, A.; Grashoff, C. *Cell. Mol. Bioeng.* **2015**, *8*, 96–105.
- (16) Piston, D. W.; Kremers, G.-J. *Trends Biochem. Sci.* **2007**, *32*, 407–414.
- (17) Autumn, K.; Liang, Y. A.; Hsieh, S. T.; Zesch, W.; Chan, W. P.; Kenny, T. W.; Fearing, R.; Full, R. J. *Nature* **2000**, *405*, 681–685.
- (18) Friedman, A. L.; Goldman, Y. E. *Biophys. J.* **1996**, *71*, 2774.
- (19) Morimatsu, M.; Mekhdjian, A. H.; Adhikari, A. S.; Dunn, A. R. *Nano Lett.* **2013**, *13*, 3985–3989.
- (20) Balaban, N. Q.; Schwarz, U. S.; Riveline, D.; Goichberg, P.; Tzur, G.; Sabanay, I.; Mahalu, D.; Safran, S.; Bershadsky, A.; Addadi, L. *Nat. Cell Biol.* **2001**, *3*, 466–472.
- (21) Atkins, P. *Shriver and Atkins' Inorganic Chemistry*; Oxford University Press, New York, 2010.
- (22) Wang, F.; Banerjee, D.; Liu, Y.; Chen, X.; Liu, X. *Analyst* **2010**, *135*, 1839–1854.
- (23) Wu, S.; Han, G.; Milliron, D. J.; Aloni, S.; Altoe, V.; Talapin, D. V.; Cohen, B. E.; Schuck, P. J. *Proc. Natl. Acad. Sci. U. S. A.* **2009**, *106*, 10917–10921.
- (24) Chatterjee, D. K.; Rufaihah, A. J.; Zhang, Y. *Biomaterials* **2008**, *29*, 937–943.
- (25) Wang, F.; Liu, X. *Chem. Soc. Rev.* **2009**, *38*, 976–989.
- (26) Tu, D.; Liu, Y.; Zhu, H.; Li, R.; Liu, L.; Chen, X. *Angew. Chem., Int. Ed.* **2013**, *52*, 1128–1133.
- (27) Aebischer, A.; Hostettler, M.; Hauser, J.; Krämer, K.; Weber, T.; Güdel, H. U.; Bürgi, H.-B. *Angew. Chem., Int. Ed.* **2006**, *45*, 2802–2806.
- (28) Renero-Lecuna, C.; Martín-Rodríguez, R.; Valiente, R.; González, J.; Rodríguez, F.; Kramer, K.; Gudel, H. *Chem. Mater.* **2011**, *23*, 3442–3448.
- (29) Tian, G.; Gu, Z.; Zhou, L.; Yin, W.; Liu, X.; Yan, L.; Jin, S.; Ren, W.; Xing, G.; Li, S.; Zhao, Y. *Adv. Mater.* **2012**, *24*, 1226–1231.
- (30) Wissler, M. D.; Chea, M.; Lin, Y.; Wu, D. M.; Mao, W. L.; Salleo, A.; Dionne, J. A. *Nano Lett.* **2015**, *15*, 1891–1897.
- (31) Zhang, Y.; Zhang, L.; Deng, R.; Tian, J.; Zong, Y.; Jin, D.; Liu, X. *J. Am. Chem. Soc.* **2014**, *136*, 4893–4896.
- (32) Wang, F.; Deng, R.; Liu, X. *Nat. Protoc.* **2014**, *9*, 1634–1644.
- (33) Mao, H.; Xu, J.-A.; Bell, P. J. *Geophys. Res.* **1986**, *91*, 4673–4676.
- (34) Solin, S.; Ramdas, A. *Phys. Rev. B* **1970**, *1*, 1687.
- (35) Tang, J.; Chen, L.; Li, J.; Wang, Z.; Zhang, J.; Zhang, L.; Luo, Y.; Wang, X. *Nanoscale* **2015**, *7*, 14752–14759.
- (36) Gnach, A.; Lipinski, T.; Bednarkiewicz, A.; Rybka, J.; Capobianco, J. A. *Chem. Soc. Rev.* **2015**, *44*, 1561–1584.
- (37) Chen, G.; Qiu, H.; Prasad, P. N.; Chen, X. *Chem. Rev.* **2014**, *114*, 5161.
- (38) Wang, F.; Han, Y.; Lim, C. S.; Lu, Y.; Wang, J.; Xu, J.; Chen, H.; Zhang, C.; Hong, M.; Liu, X. *Nature* **2010**, *463*, 1061–1065.